Ionomer self-assembly in dilute solution studied by coarse-grained molecular dynamics

Ghelichi, Mahdi; Malek, Kourosh; Eikerling, Michael H.

Publisher's version / Version de l'éditeur:
https://doi.org/10.1021/acs.macromol.5b02158
Macromolecules, 49, 4, pp. 1479-1489, 2016-02-02

Macromolecules

Article

pubs.acs.org/Macromolecules

Ionomer Self-Assembly in Dilute Solution Studied by Coarse-Grained Molecular Dynamics

Mahdi Ghelichi,[†] Kourosh Malek,[†,‡] and Michael H. Eikerling*[,†]

[†]Department of Chemistry, Simon Fraser University, 8888 University Drive, Burnaby, BC V5A 1S6, Canada

[‡]Energy, Mining, and Environment, National Research Council of Canada, 4250 Wesbrook Mall, Vancouver, BC V6T 1W5, Canada

ABSTRACT: Coarse-grained molecular dynamics simulations, reported in this article, elucidate the self-assembly of semiflexible ionomer molecules into cylindrical bundle-like aggregates. Ionomer chains are composed of hydrophobic backbones, grafted with pendant side chains that are terminated by anionic headgroups. Bundles have a core of backbones surrounded by a surface layer of charged anionic headgroups and a diffuse halo of counterions. Parametric studies of bundle properties unravel the interplay of backbone hydrophobicity, strength of electrostatic interactions between charged moieties, side chain content, and counterion valence: expectedly, the size of bundles increases with backbone hydrophobicity; the aggregate size depends nonmonotonically on the Bjerrum length; increasing the grafting density of pendant side chains results in smaller bundles; and the counterion valence exerts a strong effect on bundle size and counterion localization in the near-bundle region. Results reveal how the ionomer architecture and solvent properties influence the ionomer aggregation and associated electrostatic and mechanical bundle properties. These properties of ionomer aggregates are vital for rationalizing the water sorption behavior and transport phenomena as well as the chemical and mechanical stability of ionomer membranes.

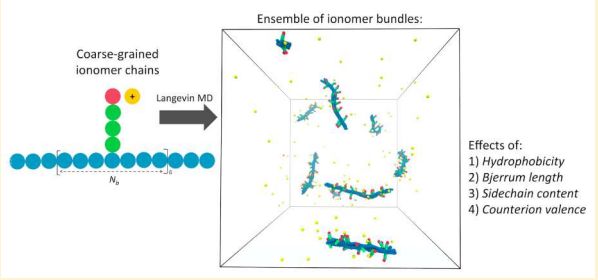

INTRODUCTION

Ionomers are moderately charged polymers with an ion content of approximately 15 mol % with respect to the amount of polymer repeat units of the backbone. The molecular architecture of ionomer moieties, ionomer density, and solvent properties determine the strengths of hydrophobic, dipolar, and ionic interactions in these systems. The interplay of these interactions results in a rich variety of structural conformations that can be classified as solution, hydrated, and melt forms. Ionomer solutions find application in paint suspensions and coating materials.[1,2] The hydrated state is encountered in electrochemical cells such as chlor-alkali cells, redox flow batteries, and polymer electrolyte fuel cells (PEFCs), where the ionomer needs to provide highly efficient and selective proton or ion transport.[3,4] Ionomer melts find major applications in battery electrolytes but also in coating technologies.[4,5]

In low-polarity solvents,[1,2] association of acid headgroups occurs due to dipolar interactions that form ionic multiples. In high-polarity solvents, acidic groups dissociate completely leading to two types of ionomer behavior based on the strength of polymer−solvent interactions. Under good solvent conditions for the polymer backbone, i.e., in a solvent that dissolves the backbone chains, solvated ionomer molecules exhibit polyelectrolyte-type behavior, forming loose ionic aggregates. In sufficiently polar solvents, ionomer backbones undergo aggregation and phase separation. This process results in the formation of a solid polymer electrolyte membrane (PEM) at high ionomer concentration.[6]

The best known PEM materials that are employed in PEFCs and PEM electrolyzers belong to the family of perfluorosulfonic acid (PFSA) ionomers, such as the famous Nafion of DuPont.[6,7] These materials consist of a strongly hydrophobic backbone with the chemical structure of Teflon and randomly attached pendant side chains of perfluorinated vinyl ethers. Side chains are terminated with sulfonic acid headgroups that are similar in acid strength to trifluoromethanesulfonic acid ("triflic" acid).[8] Under sufficiently hydrated conditions, PEMs exhibit high mechanical robustness, warranted by apolar backbone segments, as well as good water retention and high proton conductivity, conferred by the high volumetric ion density.

Studies of the structure of Nafion and assorted materials have primarily focused on the solid membrane state (with water volume fraction significantly below 50%). Using a large variety of experimental techniques, a suite of structural models have been proposed, including parallel cylinder model,[9] cluster-channel model,[10,11] lamellar[12,13] or skin-type model,[14] and rod network model.[15,16] However, none of these simplified modelistic views captures the realistic membrane structure. From a fundamental perspective, solution studies of ionomer aggregation should be highly insightful in this regard.

Based on SAXS, SANS, ESR, and ^{19}F NMR experiments,[17−22] it was conjectured that hydrophobic backbones

Received: September 30, 2015
Revised: November 27, 2015
Published: February 2, 2016

DOI: 10.1021/acs.macromol.5b02158
Macromolecules 2016, 49, 1479−1489

of Nafion form the core of self-assembled ionomer structures while ionic units are located at the periphery of this configuration. Jiang et al.[21] employed dynamic light scattering (DLS) to study the self-assembly of Nafion chains in dilute aqueous solution. Observation of stable aggregates supported the fringed-rod ionomer model proposed by Szajdzinska-Pietek et al.[23,24] These structures are similar in nature to the cylindrical-like micelles formed in solutions of semirigid synthetic polyelectrolytes such as sulfonated poly(*p*-phenylene).[25−27] Loppinet, Gebel, and others[19,20,28] studied the influence of various parameters on the self-assembling behavior in ionomer solutions. They observed that the dielectric constant of the solvent and the grafting density of pendant side chains influence the size of ionomer bundles. Using a combination of scattering and microscopy, Rubatat et al.[15,16,29] provided evidence of fibrillar (rodlike) aggregates in well-hydrated PEMs. The proton conductivity and mechanical strength of solution-cast membranes, formed from different solvents, were correlated with the properties of polymeric bundles formed in Nafion solutions.[30] Rod-like bundles have also been reported for hydrated sulfonated polyphenylene ionomers.[31] Recent studies identified aggregates of Nafion ionomer as key structure-forming elements in skin-type ionomer films, forming during self-assembly in ink mixtures of PEFC catalyst layers (CLs).[32−34]

Obviously, relatively stiff bundle-like aggregates of ionomer backbones control the properties of solid state PEMs and CLs;[6] their presence was seen to affect water sorption behavior,[35] proton conductivity,[36−38] and chemical durability.[39,40] Thus, understanding the self-assembling process of ionomers in dilute solution seems invaluable in gaining a deep insight into fundamental structure and transport properties of ionomer membranes. This insight in turn could spur the chemical design of ionomers with tailor-made properties.

The majority of simulation studies of ionomers can be categorized as either melt[41−43] or hydrated membrane simulations.[44−54] Formation and morphologies of ionic aggregates in ionomer melts as a function of counterion valence and polymer architecture have been studied with coarse-grained MD simulations.[41−43] Hydrated membrane studies have primarily focused on microphase-separated morphologies in ionomer−water mixtures of Nafion. Atomistic molecular dynamics (MD) simulations[27−32,34,37] have served as the focal point of membrane simulation studies. Other approaches such dissipative particle dynamics (DPD) simulations[50,53,55] and mean-field approaches[56] have helped expanding the time and length scale of atomistic simulations.

Self-assembly of charged polymers is a phenomenon of general interest.[33,43,50,57−72] Aggregation is often observed in biological systems[57,73] and highly charged polyelectrolytes.[68,74] Examples include fibrillar proteins[70,71] (F-actin) and DNA strands.[75,76] In these systems, self-charge attraction due to condensation of multivalent counterions is considered as the driving force of aggregation. Atomistic and coarse-grained MD simulations have been used to study self-assembly in solutions of peptide amphiphiles,[77] polyelectrolyte brushes,[67,78] and protein-like polymers[63] as well as preformed bundles of "hairy-rod" polyelectrolytes such as poly(*p*-phenylene) (PPP).[64,65,79]

Theoretical and simulation studies of hydrophobic-driven self-assembly in dilute ionomer solutions are comparatively rare in the literature. A recent theory focused on the interplay of electrostatic and hydrophobic interaction strengths in determining size and stability of cylindrical bundles of uniformly charged and closely packed rigid rods through a mean-field approach.[80]

Here we explore the self-assembly of ionomers in dilute solution through coarse-grained molecular dynamics simulations. The Ionomer Model section introduces the coarse-grained ionomer model, the type of interactions considered, and the simulation protocol. The Results section provides a systematic evaluation of ionomer bundle properties as a function of strength of hydrophobic interactions (solvent quality), strength of electrostatic interaction, ionomer side chain content, and counterion valence. Key findings are discussed in the Discussion section within the context of experimental studies of ionomer solutions and polymer electrolyte membranes.

IONOMER MODEL

In a coarse-grained model, the interacting species are groups of atoms or beads that interact via effective forces. The reduced spatial resolution of the bead representation enhances the computational efficiency. Therefore, simulations of larger systems and longer time spans can be performed, suitable for processes in biological matter[57] and heterogeneous electrochemical materials.[33,50,53,55] The task at hand is to devise a coarse-grained model that retains essential chemical and physical characteristics of the system. Figure 1 illustrates the coarse-grained ionomer architecture used in the present study.

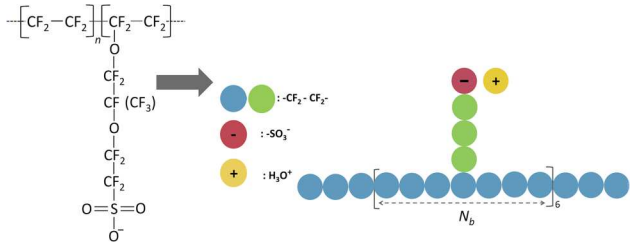

Figure 1. From atomistic structure to coarse-grained representation. In the chemical structure of Nafion ionomer in (a), *n* corresponds to six CF_2-CF_2 repeating units between side chains. In the corresponding coarse-grained representation, apolar (neutral) beads are shown in blue (backbone) and green (side chain). Anionic and counterion beads are shown in red and yellow, respectively.

Apolar beads correspond to CF_2-CF_2 units in the Nafion backbone with a diameter of $\sigma \approx 0.25$ nm. The backbone chain contains 48 beads. Regular spacing of side chains is assumed in the coarse-grained ionomer model, representing a reasonable assumption for Nafion-type ionomers, as discussed in refs 7 and 10 and references therein. A backbone segment with one grafted side chain consists of N_b apolar beads. As a reference case, we used $N_b = 7$ to resemble the chemical structure of typical Nafion ionomer with seven CF_2-CF_2 units per backbone segment, corresponding to one side chain including the junction site. The backbone strand for the reference case has six pendant side chains affixed to it ($N_s = 6$). The length of a Nafion side chain (excluding the anionic headgroup) is around 0.8 nm.[81] For the baseline case, we therefore considered side chains consisting of three apolar beads (green beads in Figure 1), giving a length of the hydrophobic side chain segment of about 0.8−1.0 nm.

We assumed complete dissociation of acid headgroups and assigned a charge of $-1e$ to terminal beads of each side chain,

DOI: 10.1021/acs.macromol.5b02158
Macromolecules 2016, 49, 1479−1489

which represent sulfonic acid headgroups, i.e., SO_3^-.[82−84] Electroneutrality of the system was achieved by adding $N_c = N_s M/Z_c$ counterions, shown as yellow beads in Figure 1, to the system, where Z_c is the counterion valence and M is the total number of ionomer chains. Initially, we considered monovalent counterions with $Z_c = +1$ e, e.g., corresponding to hydronium ions, H_3O^+, for a protonated ionomer system. As a simplification, we assumed that all beads in the system are having the same diameter, σ. No other electrolyte is added to the solution system.

Bonded interactions between beads along the ionomer backbone were represented by the bead−spring model of Kremer and Grest.[85] The connectivity of monomers in a polymer chain was maintained by the finitely extensible nonlinear elastic (FENE) potential[85−87]

$$U_{\mathrm{FENE}}(r_{ij}) = -\frac{1}{2}kR_0 \ln(1 - (r_{ij}/R_0)^2) \tag{1}$$

with spring constant $k = 30\ k_BT/\sigma^2$ and maximum extension $R_0 = 1.5\ \sigma$.[85,88,89] The flexibility of ionomer backbone and side chains was modeled using the bond angle potential

$$U_\theta(r_{ij}) = k_\theta(1 - \cos(\theta - \theta_0)) \tag{2}$$

In eq 2, k_θ is the bending rigidity and θ_0 is the equilibrium angle that is set to 180° for linear segments along backbone and side chains and to 90° at branching points. For nonbonded bead−bead interactions, we employed the standard shifted and truncated Lennard-Jones (LJ) potential

$$U_{\mathrm{LJ}}(r_{ij}) = \begin{cases} 4\varepsilon_{\mathrm{LJ}}\left[\left(\frac{\sigma}{r_{ij}}\right)^{12} - \left(\frac{\sigma}{r_{ij}}\right)^{6} - \left(\frac{\sigma}{r_c}\right)^{12} + \left(\frac{\sigma}{r_c}\right)^{6}\right], & r_{ij} < r_c \\ 0, & r_{ij} > r_c \end{cases} \tag{3}$$

where r_{ij} is the distance between beads i and j. The implicit solvent approach used in this study implies the absence of explicit interactions between polymer and solvent molecules. In this approach, hydrophobicity of ionomer groups in backbone and side chain units is embodied in the Lennard-Jones interaction parameter between apolar beads, $\varepsilon_{\mathrm{LJ}}$, which must be sufficiently attractive to adequately represent the so-called "poor-solvent" conditions.[61,64,90−92]

The cutoff distance was set to $r_c = 2.5\ \sigma$ for interactions between apolar polymer beads in the backbone and side chains. The value of $\varepsilon_{\mathrm{LJ}}$ was varied over the range specified in Table 1.

Table 1. List of System Paramters and Their Baseline Values along with the Explored Range

parameter	baseline value	parameter range explored in this work
$\varepsilon_{\mathrm{LJ}}$	1 k_BT	0.5−1.5 k_BT
λ_B	3.0 σ	1−12 σ
N_s	6	3−12
Z_c	1 e^-	1−2−3 e^-

For all other pairs of beads (apolar−anionic, apolar−cationic, anionic−anionic, anionic−cationic), we used $r_c = 2^{1/6}\sigma$ and $\varepsilon_{\mathrm{LJ}} = 1\ k_BT$. This treatment with a short cutoff distance for the interactions involving charged beads and a longer cutoff for the interactions between apolar beads allows attractive and repulsive interactions to be adequately controlled and modulated.[41−43,58,61,62,64,68,72,85,90−93] The value of $\varepsilon_{\mathrm{LJ}}$ for polymer−polymer interactions, simply referred to as $\varepsilon_{\mathrm{LJ}}$ hereafter, was varied between 0.5 k_BT and 1.5 k_BT. The baseline value $\varepsilon_{\mathrm{LJ}} = 1\ k_BT$ represents "normal hydrophobic" behavior, while $\varepsilon_{\mathrm{LJ}} = 0.5\ k_BT$ and $\varepsilon_{\mathrm{LJ}} = 1.5\ k_BT$ correspond to "weak" and "strong" hydrophobicity.[90] The θ solvent conditions correspond to $\varepsilon_{\mathrm{LJ}} = 0.33\ k_BT$.[61,90]

Charged beads interact via a direct Coulomb potential

$$U_{\mathrm{Coul}}(r_{ij}) = k_BT\frac{\lambda_B q_i q_j}{r_{ij}} \tag{4}$$

where $\lambda_B = e_0^2/4\pi\varepsilon_0\varepsilon_s k_BT$ is the Bjerrum length, e_0 is the unit charge, and ε_0 and ε_s are the permittivity of vacuum and the relative dielectric constant of the solvent. The baseline value of the Bjerrum length is $\lambda_B = 3.0\ \sigma$, which corresponds to approximately 0.7 nm in aqueous electrolyte solution ($\sigma = 0.25$ nm).

Table 1 summarizes the baseline values and the range of variations of the model parameters $\varepsilon_{\mathrm{LJ}}$, λ_B, N_s, and the counterion valence Z_c.

COMPUTATIONAL DETAILS

The particle−particle particle−mesh (PPPM)[94] with an accuracy of 10^{-5} was used for the calculation of electrostatic interactions. Simulations were carried out in the NVT ensemble with periodic boundary conditions in all three directions. A cubic box of side length $L = 110\ \sigma$ was chosen that is large enough to avoid finite size effects. The temperature was maintained through coupling of the system to a Langevin thermostat,[95] in which the motion of beads is described by

$$m_i\frac{\mathrm{d}\vec{v}_i(t)}{\mathrm{d}t} = -\nabla\vec{U}_i - \Gamma\frac{\mathrm{d}\vec{r}_i(t)}{\mathrm{d}t} + \vec{F}_i(t) \tag{5}$$

where U_i is the potential energy experienced by the ith bead with mass m_i, $\vec{F}_i(t)$ a random force with zero average value, and $\Gamma = \tau_{\mathrm{LJ}}^{-1}$ a friction coefficient calibrated to maintain a reduced temperature of $T^* = k_BT/\varepsilon_{\mathrm{LJ}}$, where τ_{LJ} is the standard LJ time, $\tau_{\mathrm{LJ}} = \sigma(m/\varepsilon_{\mathrm{LJ}})^{1/2}$. The classical Newtonian equations of motion for beads were integrated using the velocity-Verlet algorithm with a time step of $\Delta t = 0.01\ \tau_{\mathrm{LJ}}$. The time step in real units is about 15 fs considering the choice of the length scale and the chemical mapping.

Simulations were performed with LAMMPS[96] and VMD[97] was used for visualizations. The simulation protocol was as follows. A single stiff ionomer chain was placed in the middle of the simulation box and simulated for 2×10^6 time steps. The chain was then replicated and distributed on a regular 3D grid in the simulation box. The system was run for 3 million time steps under fully repulsive short-range potential. This procedure resulted in random and homogeneous distribution of chains in the simulation box. Our ensemble of $M = 25$ chains corresponds to a number density of beads of $\rho = MN/L^3 = 1.3 \times 10^{-3}\ \sigma^{-3}$ where N is the total number of beads in each chain. This density should be compared to the overlap monomer density of $\rho^* = N/(4/3\pi R_g^3)$, where R_g is the radius of gyration for a single ionomer chain. Reference conditions of $\varepsilon_{\mathrm{LJ}} = 1\ k_BT$ and $\lambda_B = 3\ \sigma$ result in $\rho^* = 1.2 \times 10^{-2}\ \sigma^{-3}$. These values indicate sufficiently dilute conditions with $\rho = 0.1\ \rho^*$.

All simulations were run for 3.5×10^7 time steps, corresponding to 0.55 μs of total simulation time. The first 3.0×10^7 time steps were used for the equilibration that is tracked by monitoring the total energy of the system as well as the gyration radius of ionomer chains. For the equilibrium state

DOI: 10.1021/acs.macromol.5b02158
Macromolecules 2016, 49, 1479−1489

analysis, data collections were performed for the last 5×10^6 time steps, and data were saved every 1.0×10^5 time steps, resulting in 50 regularly spaced snapshots.

RESULTS

Calibrating the Backbone Flexibility. As a baseline, we aimed at simulating ionomer chains with the backbone flexibility of Nafion-type ionomers. To this end, we determined k_θ by comparing the calculated persistence length, l_p, of the bare ionomer backbone (no side chains attached), simulated in the coarse-grained model, with reported values for a polytetrafluoroethylene (PTFE) chain.[9,98,99] We calculated l_p using[93,100]

$$l_p = \frac{1}{2b} \sum_{i=0}^{(N/2)-1} \langle \vec{b}_{(N/2)} \cdot \vec{b}_{(N/2)-i} + \vec{b}_{(N/2)} \cdot \vec{b}_{(N/2)+i} \rangle \quad (6)$$

where $\vec{b}_j = \vec{r}_{j+1} - \vec{r}_j$ is the jth bond vector and b is the average bond length, $b \approx 0.97\ \sigma$. Figure 2 displays values of l_p, obtained

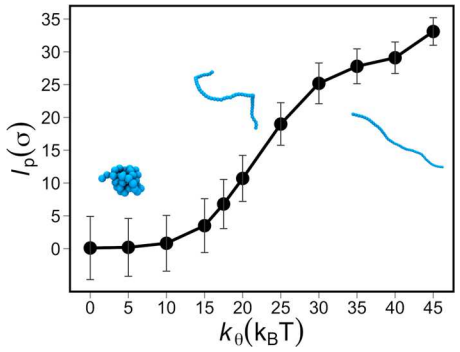

Figure 2. Calculated persistence length of single linear chain mimicking the ionomer backbone. A value of $k_\theta = 25\ k_BT$ reproduces the persistence length of a PTFE chain. The snapshots show typical chain conformations in different regimes of chain rigidity. All the error bars in this article represent the standard deviations obtained over the equilibrium trajectories.

in backbone simulations, as a function of k_θ. Reported values for the persistence length of Teflon are in the range of 2−5 nm.[9,98,99] We used the upper value of this range, $l_p = 5$ nm, which equals 20 σ in the coarse-grained ionomer model, to obtain an estimate of the corresponding k_θ value. Figure 2 shows that $k_\theta = 25\ k_BT$ produces the bending rigidity of a semiflexible chain with $l_p = 20\ \sigma$. This value was employed for k_θ in all subsequent simulations.

Effect of Ionomer Hydrophobicity. Figure 3 shows the impact of ε_{LJ} on ionomer aggregation. Starting from the random initial dispersion of chains, shown in Figure 3a, cylindrical aggregates are formed at sufficiently large values of ε_{LJ}, while a more dispersed state prevails at low values of ε_{LJ}. In aggregated structures, neutral backbone beads form the hydrophobic core region. Ionomer side chains and their anionic headgroups protrude out of the core region into the surrounding phase. Counterions form a diffuse halo around ionomer bundles. These bundle-like structures with cylindrical shape are in general agreement with cylindrical-like structures found in scattering studies of Nafion solutions.[15,19−21,28,32]

The aggregation number k, defined as the number of ionomer chains in a bundle, is calculated as the number of hydrophobic backbone beads in a single bundle divided by N. A bundle was identified as the group of monomers for which the smallest pairwise distance is less than the critical value, i.e., $r_{ij} <$

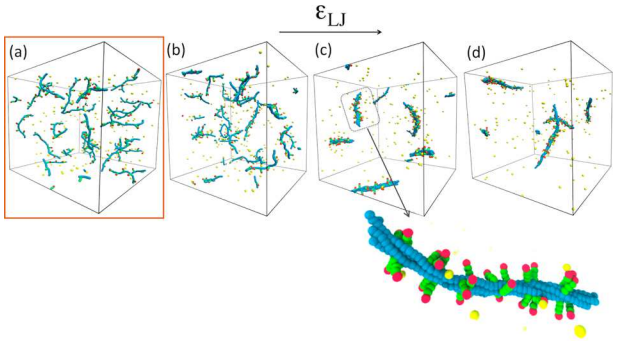

Figure 3. (a) Initial configuration of chains in the simulation box; (b) to (d) show snapshot of the self-assembled structure at different values of $\varepsilon_{LJ} = 0.5$, 1.0, and 1.5 k_BT. The color coding is the same as in Figure 2. A close-up of a typical bundle is shown below the $\varepsilon_{LJ} = 1.0\ k_BT$ box.

1.5 σ. Variation of this criterion between $r_{ij} < 1.0\ \sigma$ and $r_{ij} < 2.5\ \sigma$ did not alter the value of k. An average aggregation number $\langle k \rangle$ was calculated according to

$$\langle k \rangle = \sum_{i=1}^{M} k_i P(k_i) \quad (7)$$

where M is the total number of ionomer chains in the box. In eq 7, $P(k_i)$ is the bundle size distribution function defined as $P(k_i) = \langle N(k_i) \rangle / \sum_{i=1}^{M} \langle N(k_i) \rangle$, where $N(k_i)$ is the number of k_i bundles and $\langle ... \rangle$ denotes the time averaging over equilibrium trajectories. Figure 4a shows the variation of $\langle k \rangle$ as a function of ε_{LJ}. The dependence of $\langle k \rangle$ on ε_{LJ} is monotonic. The growth in bundle size observed upon increasing ε_{LJ} is consistent with a theory of ionomer aggregation presented in ref 80.

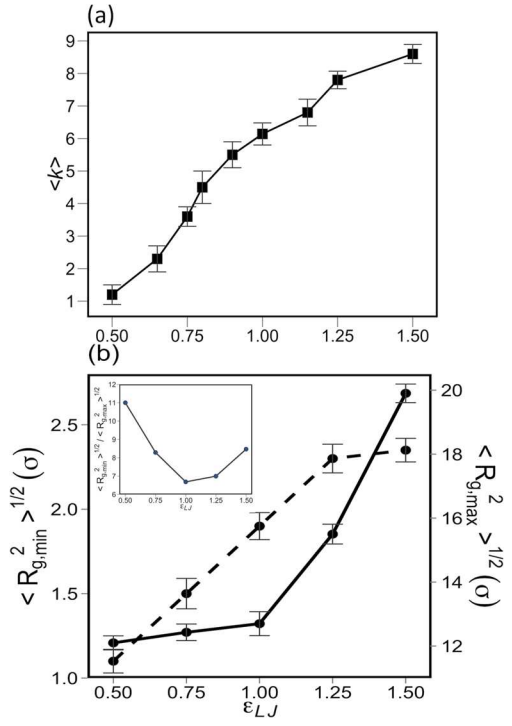

Figure 4. (a) Change in average aggregate size, $\langle k \rangle$, as a function of the interaction parameter ε_{LJ} between apolar beads. (b) Change in the minimum (radial) and maximum (longitudinal) bundle size vs ε_{LJ}. The inset shows the aspect ratio of ionomer bundles.

DOI: 10.1021/acs.macromol.5b02158
Macromolecules 2016, 49, 1479−1489

At low values, $\varepsilon_{LJ} \leq 0.75\ k_BT$, representing weak hydrophobicity of backbone chains, the increase in free energy upon bundle formation due to the loss in chain entropy outweighs the decrease in potential energy due to the aggregation of backbones; therefore, in this regime, ionomer chains remain in a dispersed state with bundle sizes of $\langle k \rangle \approx 1-2$. In the regime of large $\varepsilon_{LJ} > 1\ k_BT$, the energy loss upon aggregation of hydrophobic backbones becomes the dominant contribution to the free energy, outweighing the impact of the entropy loss and of the increase in the electrostatic interaction energy between anionic beads at the bundle surface; therefore in this regime, the equilibrium bundle size shifts to larger values.

The shape and dimension of ionomer bundles were obtained from the radius of gyration tensor ($\mathbf{S}$) of each aggregate. For every aggregate a gyration tensor is constructed that is then diagonalized to calculate the three eigenvalues, λ_1, λ_2, and λ_3. The squared gyration radius of bundles, R_g^2, would be the first invariant of $\mathbf{S}$, Tr $\mathbf{S} = \lambda_1 + \lambda_2 + \lambda_3$, while the second invariant gives the relative shape anisotropy defined as $\kappa^2 = (3S - \text{Tr } S\cdot E)/2(\text{Tr } S)^2$ with E being the unit tensor;[101−104] κ^2 ranges from 0 for a sphere ($\lambda_1 = \lambda_2 = \lambda_3$) to 1/4 for a planar symmetric object ($\lambda_1 = \lambda_2$, $\lambda_3 = 0$) and to 1 for a rod ($\lambda_2 = \lambda_3 = 0$). These eigenvalues are averaged over the ensemble of ionomer bundles in the simulation box. The imposed bending rigidity yields cylindrical ($\lambda_1 > \lambda_2 \approx \lambda_3$) ionomer bundles. The largest eigenvalue, denoted as $\langle R_{g,max}^2 \rangle^{1/2}$, corresponds to the average length of an ionomer bundle, while the average of the remaining two λ values, denoted as $\langle R_{g,min}^2 \rangle^{1/2}$, corresponds to the bundle thickness. Figure 4b shows $\langle R_{g,max}^2 \rangle^{1/2}$ and $\langle R_{g,min}^2 \rangle^{1/2}$ as functions of ε_{LJ}; the inset depicts the bundle aspect ratio $\langle R_{g,max}^2 \rangle^{1/2}/\langle R_{g,min}^2 \rangle^{1/2}$. In the range $\varepsilon_{LJ} < 1\ k_BT$, bundles grow mainly in radial direction upon increasing ε_{LJ}. At $\varepsilon_{LJ} > 1\ k_BT$, a pronounced growth trend in bundle length sets in. The plot of the aspect ratio shows a minimum at $\varepsilon_{LJ} = 1\ k_BT$. Isolation of anionic headgroups from the surrounding counterions upon further radial bundle growth would cause desolvation of anionic headgroups, causing a sudden increase in the bundle free energy.[64,65] This energetically unfavorable process that depends on the length of side chains prevents the further radial growth of bundles. It is responsible for the preferential longitudinal growth at $\varepsilon_{LJ} > 1\ k_BT$.

Detailed analyses of bundle structures involve the calculation of radial distribution functions (RDFs) of interacting beads, $g(r)$. For an isotropic system, an RDF $g_{A-B}(r)$ describes the probability of finding a particle A in a specific radial distance, r, of a reference particle B. It is defined as[105]

$$g_{A-B}(r) = \frac{V}{4\pi r^2 N_A N_B} \sum_{i=1}^{N_A} \sum_{j=1}^{N_B} \langle \delta(r - r_{ij}) \rangle \tag{8}$$

where N_A and N_B are the numbers of A and B particles in the simulated system, respectively. The triangle brackets around the δ-function indicate averaging over the equilibrium system trajectory. RDF plots presented in the following are normalized to the volume per bundle and to the number of beads of type A or B per bundle.

Figure 5 shows the RDFs of apolar backbone monomers, $g_{m-m}(r)$, anionic headgroups, $g_{h-h}(r)$, and between headgroups and counterions, $g_{h-c}(r)$, at different values of ε_{LJ}. Figure 5a shows the increase in $g_{m-m}(r)$ with increasing ε_{LJ}. This trend exhibits the enhanced aggregation of ionomer backbones as the result of an increased segregation strength. The plot furthermore reveals a dense hexagonal packing of ionomer

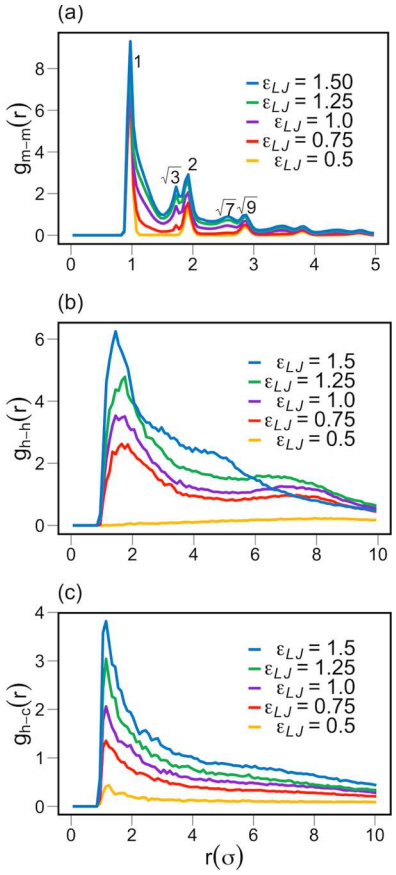

Figure 5. Radial distribution functions of (a) monomer−monomer, $g_{m-m}(r)$, (b) headgroup−headgroup, $g_{h-h}(r)$, and (c) headgroup−counterion, $g_{h-c}(r)$, at different values of ε_{LJ}. Peak location ratios are shown in (a) by considering the first peak as the reference peak.

chains in the bundle core, indicated by the ratio of peak separations in $g_{m-m}(r)$ that follows a sequence $1:\sqrt{3}:2:\sqrt{7}:\sqrt{9}$, as indicated in the plot. This hexagonal form of packing was also found in refs 17 and 19−22 for self-assembled Nafion chains in dilute solution as well as for self-assembled polyelectrolyte chains.[25]

The aggregation of backbone chains with pendant charged side chains results in the formation of ion-rich regions in solution, as can be observed in the RDFs $g_{h-h}(r)$ and $g_{h-c}(r)$, shown in Figures 5b and 5c. There is no specific correlation among headgroups in the regime of weak hydrophobicity, $\varepsilon_{LJ} = 0.5\ k_BT$. However, $g_{h-h}(r)$ grows as ε_{LJ} increases, and two correlation peaks emerge. Increasing ε_{LJ} enhances the intensity of $g_{h-h}(r)$ due to the presence of a greater number of backbone chains in the bundle, which results in a greater total number of anionic headgroups at the bundle surface. The locations of the first and second peak are not altered for $\varepsilon_{LJ} = 0.75\ k_BT$, $1\ k_BT$, and $1.25\ k_BT$. However, these peaks are shifted to smaller values, indicating a densification of surface groups, in the case of strong hydrophobicity, i.e., for $\varepsilon_{LJ} = 1.5\ k_BT$.

The RDF $g_{h-c}(r)$, depicted in Figure 5c for various values of ε_{LJ}, reveals that the counterion localization in the vicinity of headgroups increases with ε_{LJ}. A higher charge density and a greater surface potential in bundles with stronger hydrophobic interactions induces stronger electrostatic attraction on counterions. This stronger interaction results in a greater localization of counterions around bundles. Further inspection

DOI: 10.1021/acs.macromol.5b02158
Macromolecules 2016, 49, 1479−1489

of Figure 3 affirms the formation of a counterion cloud at the bundle surface in the regime of strong hydrophobicity.

Effect of Electrostatic Interaction Strength. In this section, we explore the changes in aggregation behavior upon variation of λ_B, while fixing $\varepsilon_{LJ} = 1\ k_BT$. The change of λ_B in experiment can be achieved through variation of the dielectric constant of the solvent. In all simulations performed with varying values of λ_B the formation of cylindrical bundles was observed.

The nonmonotonic behavior in the plot of $\langle k \rangle$ vs λ_B in Figure 6a can be explained as follows: the decreasing trend for

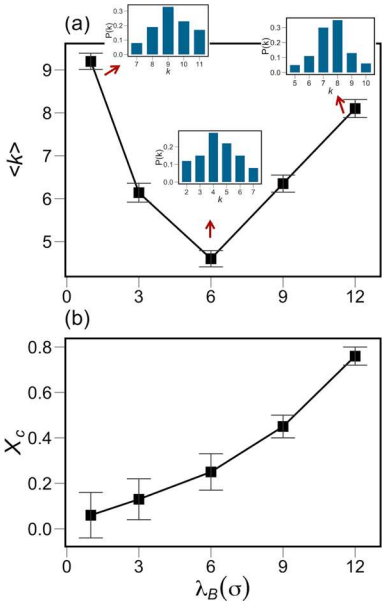

Figure 6. (a) Dependence of average bundle size on the value of λ_B. Imbedded plots show the distribution function of the bundle number vs k for $\lambda_B = 1\ \sigma$, $6\ \sigma$, and $12\ \sigma$; (b) shows the fraction of counterions within $2.5\ \sigma$ of the anionic headgroups.

$\lambda_B < 6\ \sigma$ is caused by the electrostatic repulsion of anionic charges on the bundle surface that disfavors aggregation; however, at large values of λ_B, for $\lambda_B > 6\ \sigma$, the trend is reversed due to the effect of counterion localization shown in Figure 6b. The fraction of localized counterions, X_c, is defined as the number of counterions in radial distance $<2.5\ \sigma$ of the nearest headgroup.[67,78] X_c is an increasing function of λ_B. Counterion localization results in an effective screening of the anionic charges and a correspondingly reduced effective Coulomb repulsions between headgroups.

For $\lambda_B < 6\ \sigma$, the majority of counterions remain dispersed (nonlocalized) in the electrolyte. In this regime of weak counterion localization, the free energy change upon increasing λ_B is mainly determined by the increasing electrostatic repulsion between anionic headgroups. This dependence disfavors aggregation, which is responsible for the decrease in $\langle k \rangle$ with λ_B and the evolution of a more dispersed ionomer solution, as shown by the changes in the size distribution functions shifting from λ_B values of $1\ \sigma$ to $6\ \sigma$.

At $\lambda_B > 6\ \sigma$, the effect of counterion localization overcompensates the increase in the direct Coulomb interaction between headgroups, leading to a net decrease in the effective electrostatic energy with increasing λ_B and growing $\langle k \rangle$, and formation of a phase-separated ionomer solution. A nonmonotonic dependence on Bjerrum length was also observed in refs 67 and 78 for the variation in the thickness of polyelectrolyte brushes.

Figure 7 shows the RDF of backbone monomers for the range of explored λ_B values. $g_{m-m}(r)$ demonstrates a non-

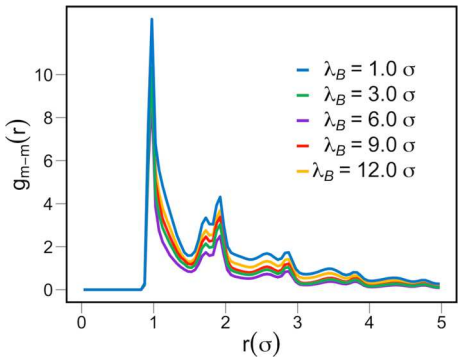

Figure 7. Monomer−monomer RDF $g_{m-m}(r)$ for different values of the Bjerrum length.

monotonic dependence on λ_B. The spatial ordering of the ionomer chains in the bundle core is retained for the explored values of the Bjerrum length. Ionomer bundles with the smallest λ_B ($\lambda_B = 1\ \sigma$) exhibit the largest magnitude of peaks in $g_{m-m}(r)$. The RDF $g_{m-m}(r)$ decreases as λ_B increases to $6\ \sigma$. Further increase in λ_B above $6\ \sigma$ results in an upsurge in $g_{m-m}(r)$. These trends are consistent with the trends in the bundle size reported in Figure 6a.

Effect of Side Chain Density. The effect of the side chain density on the aggregation behavior of ionomer chains is studied by increasing the number of grafting sites, N_s, at fixed length of the ionomer backbone. Figure 8 shows the solution of

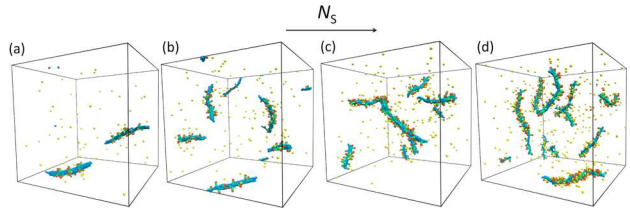

Figure 8. Snapshots showing the ionomer bundles at different values of N_s: (a) $N_s = 3$, (b) $N_s = 6$, (c) $N_s = 9$, (d) $N_s = 15$.

ionomer aggregates for $N_s = 3, 6, 9, 15$ with fixed $\varepsilon_{LJ} = 1\ k_BT$ and $\lambda_B = 3\ \sigma$. Increasing N_s is accompanied by the formation of a larger number of aggregates with smaller sizes.

Figure 9a shows the dependence of the bundle size on N_s. Larger N_s results in shorter distance among the anionic headgroups. The decrease in $\langle k \rangle$ with increasing N_s, seen in Figure 9a, can be attributed to the enhanced electrostatic repulsion between anionic headgroups that increases the bundle free energy and disfavors aggregation. The size distribution functions also clearly show the shift of the ionomer ensemble from a phase-separated system of large aggregates to a system consisting of small ionomer bundles.

Figure 9b shows the increase of the Coulomb interaction energy of headgroups (per headgroup) as a function of N_s. This interaction energy is obtained by isolating the electrostatic and short-range portions of the mutual headgroup interactions.

Figure 9c shows the change in the longitudinal and radial bundle dimension as a function of N_s. The decrease in the

DOI: 10.1021/acs.macromol.5b02158
Macromolecules 2016, 49, 1479−1489

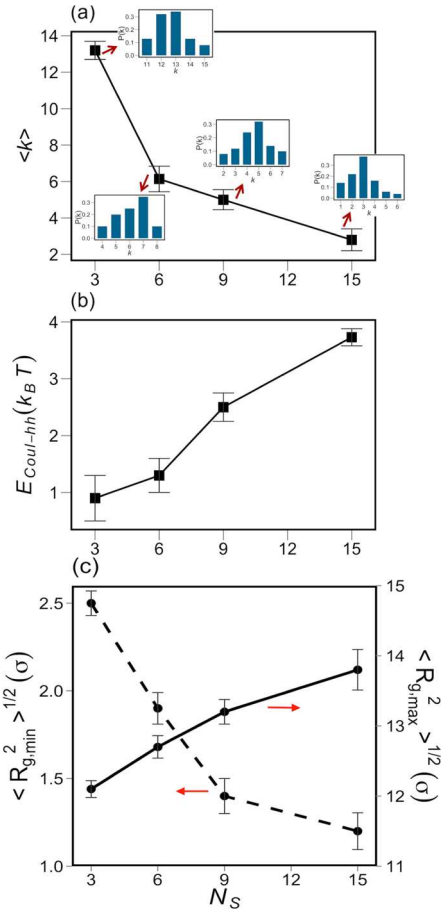

Figure 9. Effect of N_s on (a) equilibrium aggregate size, $\langle k \rangle$ (imbedded plots show the distribution function of the bundle number vs k), (b) Coulombic energy of anionic headgroups, and (c) maximum and minimum bundle gyration radius.

$\langle R_{g,min}^2 \rangle^{1/2}$ follows the same trend as $\langle k \rangle$. An increase in $\langle R_{g,max}^2 \rangle^{1/2}$, in the range 2 σ, occurs upon increasing N_s from 3 to 15. This range of variation in the bundle length mostly originates from the Coulombic-induced chain stretching upon increasing the number of pendant ionic side chains.

Figure 10 displays the RDFs among headgroup units for the final aggregated structures at different N_s. Bundles formed from chains with smaller N_s are more populated of headgroups than the bundles formed from chains with greater N_s values. The observed trend in $g_{h-h}(r)$ is attributed to the larger bundles that form from ionomer chains with fewer side chains.

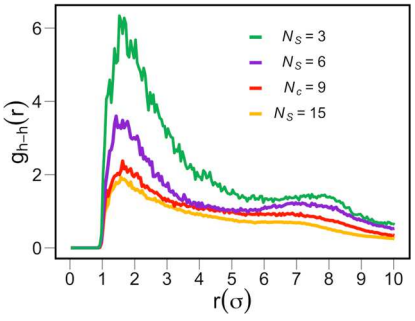

Figure 10. Radial distribution function among anionic headgroups, $g_{h-h}(r)$, for the explored values of N_s.

The side chain content in commercial PFSAs such as 3M, Hyflon, and Nafion is primarily expressed in terms of the ion exchange capacity (IEC) of the polymer membrane, defined as the number of moles of acid groups over the mass of dry membrane. Major dissimilarity in PFSA ionomers with different side chain chemistries is manifested in terms of their different side chain contents. The side chain lengths of ionomer materials such as 3M, Hyflon, and Nafion vary in the range from 5.27 to 8.44 Å.[81] We simulated systems with l_s varying from 1 σ to 6 σ. We did not find any clearly discernible trend in bundle size as a function of l_s. The length of side chains has however a strong impact on the dynamics of individual ionomer chains; therefore, over the simulation time of 3.5×10^7 time steps, no equilibration was observed for ionomer systems with l_s = 6 σ. We will discuss the impact of the side chain length on ionomer properties in a forthcoming publication.

Effect of Counterion Valence. The effect of the counterion valence on the aggregation behavior of ionomer chains was investigated by comparing results for Z_c = +1, +2, and +3. Figure 11 depicts the final snapshots for the systems

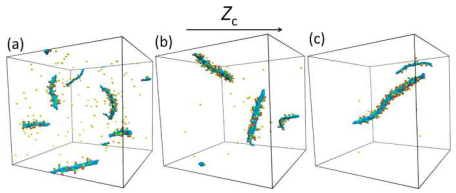

Figure 11. Morphologies of ionomer solutions for solutions containing (a) monovalent, Z_c = +1, (b) divalent, Z_c = +2, and (c) trivalent, Z_c = +3, counterions.

with different counterion valences. As Z_c increases, the solution contains fewer but larger ionomer bundles. In the case of trivalent counterions, we can see the formation of a weakly bent and elongated worm-like bundle. The localization of counterions in the vicinity of ionomer bundles increases dramatically with Z_c because of the stronger electrostatic attraction of multivalent counterions to the anionic headgroups. This trend is clearly observed in Figure 11 where almost all the counterions are strongly localized near the anionic headgroups for Z_c = +3.

The enhanced localization results in screening the repulsion of anionic headgroups, thereby enabling the growth of larger bundles. Strong localization of multivalent counterions also induces an attractive interaction[106] among charged units known as the bridging[107] effect. Figure 12a shows that $\langle k \rangle$ increases significantly with Z_c. Figure 12b shows that the fraction of strongly localized counterions (within 2.5 σ), X_c, increases monotonously with Z_c. Figure 12c reveals a 2-fold increase in average bundle length and an increase by 0.8 σ in the bundle thickness with Z_c. This observation points out the preferential longitudinal assembly and growth of ionomer bundles upon increase in Z_c.

It is interesting to analyze the influence of counterion valence on the dynamics of backbone monomers and counterions by calculating the mean-square displacement (MSD) of these species. The MSD is calculated according to

$$\mathrm{MSD}(t) = \langle |r_i(t) - r_i(0)|^2 \rangle \quad (9)$$

after subtracting the center of mass of the corresponding beads. Figure 13 shows the MSD of counterions and backbone monomer beads during the simulation for different Z_c. Figure

DOI: 10.1021/acs.macromol.5b02158
Macromolecules 2016, 49, 1479−1489

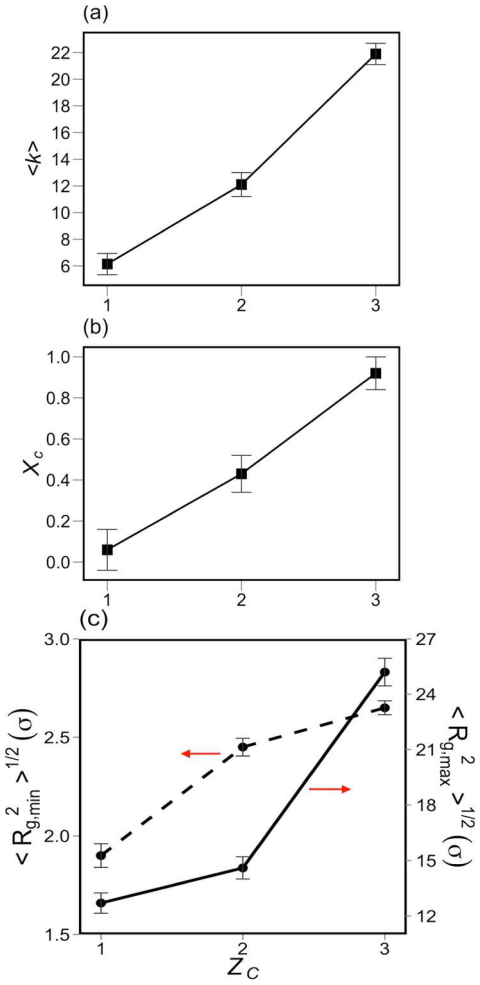

Figure 12. Effect of counterion valence Z_c on (a) average bundle sizes, (b) fraction of localized counterions, and (c) effective length and diameter of bundles.

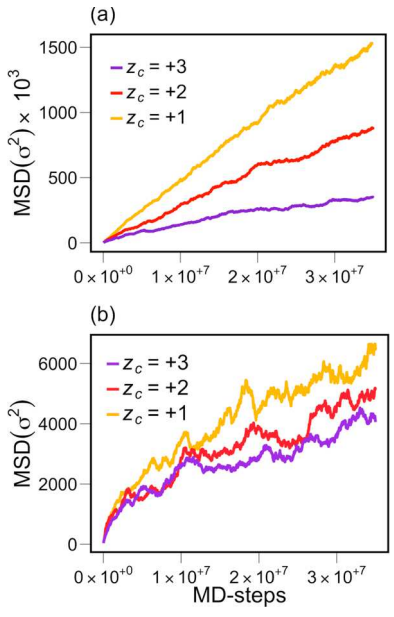

Figure 13. (a) MSD of counterions with different valences and (b) changes in MSD of backbone monomer beads for bundles formed in the presence of counterion with different valence Z_c.

13a reveals that the strong localization of counterions for Z_c = +3 markedly diminishes their mobility. The backbone dynamics is also slowed down with increased Z_c because of the larger number of chains in the bundle core and the increased number of monomer−monomer contacts. Yan et al.[69] also observed the decrease in the counterion dynamics upon increasing its valency due to stronger bonding to the polyelectrolyte.

DISCUSSION

We have systematically explored the impact of primary parameters of the ionomer−solvent system on the aggregation behavior of ionomer molecules in dilute solution. Here, we will reiterate the main trends and evaluate them in comparison to experimental findings reported in the literature.

Simulation results suggest that aggregation numbers of PFSA-type ionomers can be expected to lie in the range of $\langle k \rangle$ = 6−10, as seen in Figures 4, 6a, 9a, and 12a for our reference set of parameters. This range is consistent with stable aggregate sizes of k = 9 that the theory of ionomer aggregation presented in ref 80 predicted for a set of baseline parameters that corresponds to PFSA ionomers in aqueous solution.

Increased hydrophobicity resulted in the formation of larger bundles. A change in the strength of the hydrophobic interactions between apolar polymer beads, represented in the model by the parameter ε_{LJ}, can be induced through alteration of the ionomer chemistry, for instance, by replacing fluorocarbon with hydrocarbon chains. Less hydrophobic hydrocarbon ionomers exhibit smaller values of ε_{LJ} that diminish the tendency for bundle formation, resulting in more dispersed solution characteristics. Comparative experimental investigation of the solution features of hydrocarbon and PFSA ionomers would be highly insightful in this regard.

The second major parametric effect refers to the grafting density of side chains. In the model study it is evaluated by varying the number N_s of side chains per ionomer backbone chain (with fixed length). We observed in Figure 9a that an increase in N_s results in a monotonic decrease in bundle size, leading to a dispersed ionomer state in the limit of high N_s. The ionic content of ionomers is controlled during the synthesis process. Experimental studies of Loppinet and Gebel[19] confirm the decrease in bundle size in solutions of PFSA-type ionomers with higher side chain content. A similar decreasing trend in aggregation behavior was seen in SAXS studies by Rulkens et al.[25] performed on solutions of semirigid poly(*p*-phenylene)s (PPP) chains upon increasing the sulfonate ion content. In the limit of very high ionic content such systems assumed the configuration of nonaggregating and dispersed polyelectrolyte chains.

A way to isolate the impact of direct Coulomb interactions on ionomer aggregation is to add salt ions to the solution that screen the electric charges and reduce the value of λ_B. Jiang et al.[21] studied the size of Nafion bundles in solution at different salt contents. Increasing the salt concentration resulted in an increase in the size of Nafion bundles, consistent with the trend seen in Figure 6a at low λ_B. Experimental studies exploring regimes of strong electrostatic interactions are needed to capture the predicted nonmonotonic dependence of the bundle size on the strength of electrostatic interactions.

Employing solvents with different dielectric properties exerts a more complex impact on the aggregation behavior. In simulations, changes in solvent properties affect the interplay between solvent-mediated interactions of apolar ionomer groups, embodied in the simulation parameter ε_{LJ}, and direct

DOI: 10.1021/acs.macromol.5b02158
Macromolecules 2016, 49, 1479−1489

Coulomb interactions, embodied in the Bjerrum length, λ_B. A less polar solvent will decrease the value of ε_{LJ} for the hydrophobic ionomer, thus disfavoring the aggregation of backbones, and increase the value of λ_B, representing an increase in the strength of direct Coulomb interactions. Looking at Figure 6a, we should distinguish two regimes. In the regime of small λ_B, i.e., $\lambda_B < 6\ \sigma$, Coulomb interactions of anionic headgroups are weakly screened by diffuse counterions. In this regime of weak counterion localization, the less polar solvent causes consistent trends in aggregation behavior exerted by ε_{LJ} and λ_B: the net effect is a decrease in $\langle k \rangle$ for the less polar solvent. In the regime of high λ_B, i.e. $\lambda_B > 6\ \sigma$, the screening effect due to strong counterion localization in the vicinity of bundles comes into play, reverting the impact of solvent polarity on effective electrostatic interactions. In this regime of strong counterion localization, the impacts of variations in ε_{LJ} and λ_B on ionomer aggregation oppose each other: the less polar solvent tends to weaken aggregation via ε_{LJ} and enhance aggregation via λ_B; a general trend of the net effect cannot be predicted.

Loppinet et al.[19,20] observed, using SAXS and SANS, that the radius of rod-like Nafion aggregates increased when more polar solvents that are solvents with higher dielectric constant and greater ε_{LJ} were employed. They observed a shift in the ionomer peak to lower q values for aqueous solvents compared to alcoholic solvents (with $\lambda_b \approx 9\ \sigma$ by considering $\varepsilon \approx 25$), indicating larger radius of ionomer aggregates in solvents with higher polarity. Consistently, a decrease in aggregate size of Nafion ionomer was seen by Welch et al.[108] when water was replaced with glycerol, a less polar solvent. These trends are in accord with the trends predicted by simulations in the regime of weak counterion localization.

Experimentally, there is no direct study regarding the influence of counterion valency on the colloidal aggregation of hydrophobic ionomer chains or PFSA chains in dilute solution. On the membrane level, counterion valence was seen to have a strong impact on the mechanical properties of the ionomer membrane.[45,109] These changes can possibly originate from the fundamental structural reorganization at the bundle level. However, trying to relate these membrane studies to our solution-based simulations would be speculative at this point.

CONCLUSION

In this study, we have applied coarse-grained molecular dynamics simulations to study the aggregation of ionomer chains in dilute solution with no added electrolyte. Simulations account for the short-range interactions of apolar hydrophobic polymer groups in ionomer backbone and side chains as well as explicit Coulomb indications between charged moieties, viz. anionic headgroups and counterions in solution. The interplay of these interactions controls the formation of ionomer aggregates or bundles of finite size. Stable bundles attain a cylindrical-like shape with dense hexagonal packing arrangement of ionomer backbones. The size of stable bundles, the density of anionic headgroups at their surface, and the distribution of counterions in the surrounding solution depend on the primary ionomer chemistry and architecture, viz., the chemical nature of polymer groups, the grafting density of side chains, and the properties of the solvent. We found that a stronger backbone hydrophobicity of polymer groups results in larger bundle sizes. Increasing the grafting density of acid-terminated side chains leads to a monotonic decrease in bundle size. A variation in the strength of Coulomb interactions gives rise to a nonmonotonic trend in bundle size: in a regime of weak counterion localization, corresponding to a small Coulomb interaction parameter, bundle size decreases with increasing interaction strength; in a regime of strong counterion localization, attained for large Coulomb interaction parameter, the bundle size increases with increasing interaction strength. Ionomers with higher number of pendant groups form smaller bundles due to stronger electrostatic repulsion among their anionic moieties. Increasing the valence of counterions from one to three results in a pronounced increase in bundle size, and more strikingly it leads to an almost complete depletion of the solution from counterions owed to pronounced counterion condensation at the bundle surface. This effect is expected to have a strong impact on ion transport phenomena in the membrane. Generally, trends predicted based on our computational study are consistent with experimental observations. The ability to correlate primary ionomer parameters and solvent properties with the structure and electrostatic properties of ionomer bundles is crucial for a rational design of membrane-forming materials. In related work, we study how the mechanical and electrostatic properties of microscopic bundles determine water sorption and swelling, transport phenomena, chemical degradation, and mechanical failure of ionomer-based membranes. The present work is a vital step toward a basic understanding on how to modify ionomer and solvent properties in order to obtain polymer electrolyte membranes with improved performance and stability.

AUTHOR INFORMATION

Corresponding Author

*E-mail: meikerl@sfu.ca (M.H.E.).

Notes

The authors declare no competing financial interest.

ACKNOWLEDGMENTS

The work reported in this manuscript was performed with the financial support from an NSERC Discovery Grant, entitled *Materials for Electrochemical Energy Conversion: From Fundamental Physics to Advanced Design*. Simulations were performed using the Grex computational facility at the University of Manitoba, provided through WestGrid and Compute Canada.

REFERENCES

(1) Nomula, S.; Cooper, S. L. *Macromolecules* **2001**, *34*, 2653−2659.
(2) Nomula, S.; Cooper, S. L. *J. Phys. Chem. B* **2000**, *104*, 6963−6972.
(3) Schlick, S. *Ionomers: Characterization, Theory, and Applications*; CRC Press: Boca Raton, FL, 1996.
(4) Eisenberg, A.; Kim, J.-S. *Introduction to Ionomers*; John Wiley & Sons: New York, 1998.
(5) Zhang, L.; Brostowitz, N. R.; Cavicchi, K. A.; Weiss, R. A. *Macromol. React. Eng.* **2014**, *8*, 81−99.
(6) Eikerling, M.; Kulikovsky, A. *Polymer Electrolyte Fuel Cells: Physical Principles of Materials and Operation*; CRC Press: Boca Raton, FL, 2014.
(7) Grot, W. G. *Macromol. Symp.* **1994**, *82*, 161−172.
(8) Eikerling, M.; Paddison, S. J.; Zawodzinski, T. A. *J. New Mater. Electrochem. Syst.* **2002**, *5*, 15−23.
(9) Schmidt-Rohr, K.; Chen, Q. *Nat. Mater.* **2008**, *7*, 75−83.
(10) Mauritz, K. A.; Moore, R. B. *Chem. Rev.* **2004**, *104*, 4535−4585.
(11) Gierke, T. D. .; Munn, G. E. .; Wilson, F. C. *J. Polym. Sci., Polym. Phys. Ed.* **1981**, *19*, 1687−1704.
(12) Litt, M. H. *Polym. Prepr.* **1997**, *38*, 80−81.

DOI: 10.1021/acs.macromol.5b02158
Macromolecules 2016, 49, 1479−1489

(13) Haubold, H. G.; Vad, T.; Jungbluth, H.; Hiller, P. *Electrochim. Acta* **2001**, *46*, 1559−1563.
(14) Berrod, Q.; Lyonnard, S.; Guillermo, A.; Ollivier, J.; Frick, B.; Manseri, A.; Améduri, B.; Gébel, G. *Macromolecules* **2015**, *48*, 6166−6176.
(15) Rubatat, L.; Rollet, A. L.; Gebel, G.; Diat, O. *Macromolecules* **2002**, *35*, 4050−4055.
(16) Rubatat, L.; Gebel, G.; Diat, O. *Macromolecules* **2004**, *37*, 7772−7783.
(17) Aldebert, P.; Dreyfus, B.; Pineri, M. *Macromolecules* **1986**, *19*, 2651−2653.
(18) Rollet, A. L.; Gebel, G.; Simonin, J. P.; Turq, P. *J. Polym. Sci., Part B: Polym. Phys.* **2001**, *39*, 548−558.
(19) Loppinet, B.; Gebel, G. *Langmuir* **1998**, *14*, 1977−1983.
(20) Loppinet, B.; Gebel, G.; Williams, C. E. *J. Phys. Chem. B* **1997**, *101*, 1884−1892.
(21) Jiang, S.; Xia, K.-Q.; Xu, G. *Macromolecules* **2001**, *34*, 7783−7788.
(22) Aldebert, P.; Dreyfus, B.; Gebel, G.; Nakamura, N.; Pineri, M.; Volino, F. *J. Phys. (Paris)* **1988**, *49*, 2101−2109.
(23) Szajdzinska-Pietek, E.; Schlick, S.; Plonka, A. *Langmuir* **1994**, *10*, 1101−1109.
(24) Szajdzinska-Pietek, E.; Schlick, S.; Plonka, A. *Langmuir* **1994**, *10*, 2188−2196.
(25) Rulkens, R.; Wegner, G.; Thurn-Albrecht, T. *Langmuir* **1999**, *15*, 4022−4025.
(26) Kroeger, A.; Deimede, V.; Belack, J.; Lieberwirth, I.; Fytas, G.; Wegner, G. *Macromolecules* **2007**, *40*, 105−115.
(27) Zaroslov, Y. D.; Gordeliy, V. I.; Kuklin, A. I.; Islamov, A. H.; Philippova, O. E.; Khokhlov, A. R.; Wegner, G. *Macromolecules* **2002**, *35*, 4466−4471.
(28) Gebel, G.; Loppinet, B.; Hara, H.; Hirasawa, E. *J. Phys. Chem. B* **1997**, *101*, 3980−3987.
(29) Rubatat, L.; Diat, O. *Macromolecules* **2007**, *40*, 9455−9462.
(30) Lin, H. L.; Yu, T. L.; Huang, C. H.; Lin, T. L. *J. Polym. Sci., Part B: Polym. Phys.* **2005**, *43*, 3044−3057.
(31) He, L.; Fujimoto, C. H.; Cornelius, C. J.; Perahia, D. *Macromolecules* **2009**, *42*, 7084−7090.
(32) Paul, D. K.; Karan, K.; Docoslis, A.; Giorgi, J. B.; Pearce, J. *Macromolecules* **2013**, *46*, 3461−3475.
(33) Malek, K.; Eikerling, M.; Wang, Q.; Navessin, T.; Liu, Z. *J. Phys. Chem. C* **2007**, *111*, 13627−13634.
(34) Yamaguchi, M.; Matsunaga, T.; Amemiya, K.; Ohira, A.; Hasegawa, N.; Shinohara, K.; Ando, M.; Yoshida, T. *J. Phys. Chem. B* **2014**, *118*, 14922−14928.
(35) Eikerling, M. H.; Berg, P. *Soft Matter* **2011**, *7*, 5976−5990.
(36) Eikerling, M.; Kornyshev, A. A.; Kuznetsov, A. M.; Ulstrup, J.; Walbran, S. *J. Phys. Chem. B* **2001**, *105*, 3646−3662.
(37) Eikerling, M.; Kornyshev, A. A.; Spohr, E. In *Fuel Cells I*; Springer: Berlin, 2008; Vol. *215*, pp 15−54.
(38) Vartak, S.; Roudgar, A.; Golovnev, A.; Eikerling, M. *J. Phys. Chem. B* **2013**, *117*, 583−588.
(39) Ghelichi, M.; Melchy, P.-É. A.; Eikerling, M. H. *J. Phys. Chem. B* **2014**, *118*, 11375−11386.
(40) Rodgers, M. P.; Bonville, L. J.; Kunz, H. R.; Slattery, D. K.; Fenton, J. M. *Chem. Rev.* **2012**, *112*, 6075−6103.
(41) Hall, L. M.; Seitz, M. E.; Winey, K. I.; Opper, K. L.; Wagener, K. B.; Stevens, M. J.; Frischknecht, A. L. *J. Am. Chem. Soc.* **2012**, *134*, 574−587.
(42) Hall, L. M.; Stevens, M. J.; Frischknecht, A. L. *Macromolecules* **2012**, *45*, 8097−8108.
(43) Goswami, M.; Kumar, S. K.; Bhattacharya, A.; Douglas, J. F. *Macromolecules* **2007**, *40*, 4113−4118.
(44) Cui, S.; Liu, J.; Selvan, M. E.; Keffer, D. J.; Edwards, B. J.; Steele, W. V. *J. Phys. Chem. B* **2007**, *111*, 2208−2218.
(45) Daly, K. B.; Panagiotopoulos, A. Z.; Debenedetti, P. G.; Benziger, J. B. *J. Phys. Chem. B* **2014**, *118*, 13981−13991.
(46) Knox, C. K.; Voth, G. A. *J. Phys. Chem. B* **2010**, *114*, 3205−3218.
(47) Lucid, J.; Meloni, S.; Mackernan, D.; Spohr, E.; Ciccotti, G. *J. Phys. Chem. C* **2013**, *117*, 774−782.
(48) Urata, S.; Irisawa, J.; Takada, A.; Shinoda, W.; Tsuzuki, S.; Mikami, M. *J. Phys. Chem. B* **2005**, *109*, 4269−4278.
(49) Jang, S. S.; Molinero, V.; Cagin, T.; Goddard, W. A., III *J. Phys. Chem. B* **2004**, *108*, 3149−3157.
(50) Vishnyakov, A.; Neimark, A. V. *J. Phys. Chem. B* **2014**, *118*, 11353−11364.
(51) Hristov, I. H.; Paddison, S. J.; Paul, R. *J. Phys. Chem. B* **2008**, *112*, 2937−2949.
(52) Wang, C.; Paddison, S. J. *Soft Matter* **2014**, *10*, 819−830.
(53) Yamamoto, S.; Hyodo, S.-A. *Polym. J.* **2003**, *35*, 519−527.
(54) Vishnyakov, A.; Neimark, A. V. *J. Phys. Chem. B* **2001**, *105*, 9586−9594.
(55) Malek, K.; Eikerling, M.; Wang, Q.; Liu, Z.; Otsuka, S.; Akizuki, K.; Abe, M. *J. Chem. Phys.* **2008**, *129*, 204702−204710.
(56) Komarov, P. V.; Veselov, I. N.; Chu, P. P.; Khalatur, P. G. *Soft Matter* **2010**, *6*, 3939−3956.
(57) Adamcik, J.; Mezzenga, R. *Macromolecules* **2012**, *45*, 1137−1150.
(58) Karatasos, K. *Macromolecules* **2008**, *41*, 1025−1033.
(59) Srinivas, G.; Shelley, J. C.; Nielsen, S. O.; Discher, D. E.; Klein, M. L. *J. Phys. Chem. B* **2004**, *108*, 8153−8160.
(60) Wang, S.; Larson, R. G. *Langmuir* **2015**, *31*, 1262−1271.
(61) Grest, G. S.; Murat, M. *Macromolecules* **1993**, *26*, 3108−3117.
(62) Hall, L. M.; Stevens, M. J.; Frischknecht, A. L. *Phys. Rev. Lett.* **2011**, *106*, 1−4.
(63) Khalatur, P. G.; Khokhlov, A. R.; Mologin, D. A.; Reineker, P. *J. Chem. Phys.* **2003**, *119*, 1232−1247.
(64) Limbach, H. J.; Holm, C.; Kremer, K. *Macromol. Chem. Phys.* **2005**, *206*, 77−82.
(65) Limbach, H. J.; Sayar, M.; Holm, C. *J. Phys.: Condens. Matter* **2004**, *16*, S2135−S2144.
(66) Omar, A. K.; Hanson, B.; Haws, R. T.; Hu, Z.; Bout, D. A.; Vanden; Rossky, P. J.; Ganesan, V. *J. Phys. Chem. B* **2015**, *119*, 330−337.
(67) Sandberg, D. J.; Carrillo, J. M. Y.; Dobrynin, A. V. *Langmuir* **2009**, *25*, 13158−13168.
(68) Stevens, M. J. *Phys. Rev. Lett.* **1999**, *82*, 101−104.
(69) Yan, L.-T.; Guo, R. *Soft Matter* **2012**, *8*, 660.
(70) Wong, G. C.; Tang, J. X.; Lin, A.; Li, Y.; Janmey, P. A.; Safinya, C. R. *Science* **2000**, *288*, 2035−2039.
(71) Tang, J. X.; Janmey, P. A. *J. Biol. Chem.* **1996**, *271*, 8556−8563.
(72) Vasilevskaya, V. V.; Markov, V. A.; Ten Brinke, G.; Khokhlov, A. R. *Macromolecules* **2008**, *41*, 7722−7728.
(73) Morriss-Andrews, A.; Shea, J. E. *J. Phys. Chem. Lett.* **2014**, *5*, 1899−1908.
(74) Mohammadinejad, S.; Fazli, H.; Golestanian, R. *Soft Matter* **2009**, *5*, 1522−1529.
(75) Goobes, R.; Cohen, O.; Minsky, A. *Nucleic Acids Res.* **2002**, *30*, 2154−2161.
(76) Rogers, P. H.; Michel, E.; Bauer, C. A.; Vanderet, S.; Hansen, D.; Roberts, B. K.; Calvez, A.; Crews, J. B.; Lau, K. O.; Wood, A.; Pine, D. J.; Schwartz, P. V. *Langmuir* **2005**, *21*, 5562−5569.
(77) Fu, I. W.; Markegard, C. B.; Chu, B. K.; Nguyen, H. D. *Langmuir* **2014**, *30*, 7745−7754.
(78) Carrillo, J. M. Y.; Dobrynin, A. V. *Langmuir* **2009**, *25*, 13158−13168.
(79) Hess, B.; Sayar, M.; Holm, C. *Macromolecules* **2007**, *40*, 1703−1707.
(80) Melchy, P. É. A.; Eikerling, M. H. *Phys. Rev. E* **2014**, *89*, 032603−032609.
(81) Clark, J. K.; Paddison, S. J. *J. Phys. Chem. A* **2013**, *117*, 10534−10543.
(82) Choi, P.; Jalani, N. H.; Datta, R. *J. Electrochem. Soc.* **2005**, *115*, E123−E130.
(83) Zhang, C.; Knyazev, D. G.; Vereshaga, Y. A.; Ippoliti, E.; Nguyen, T. H.; Carloni, P.; Pohl, P. *Proc. Natl. Acad. Sci. U. S. A.* **2012**, *109*, 9744−9749.

DOI: 10.1021/acs.macromol.5b02158
Macromolecules 2016, 49, 1479−1489

(84) Marcus, Y. *J. Chem. Phys.* **2012**, *137*, 154501.
(85) Kremer, K.; Grest, G. S. *J. Chem. Phys.* **1990**, *92*, 5057−5086.
(86) Binder, K. *Monte Carlo and Molecular Dynamics Simulations in Polymer Science*; Oxford University Press: New York, 1995.
(87) Kotelyanskii, M.; Theodorou, D. N. *Simulation Methods for Polymers*; CRC Press: Boca Raton, FL, 2004.
(88) Dunweg, B.; Kremer, K. *J. Chem. Phys.* **1993**, *99*, 6983−6997.
(89) Binder, K. *Monte Carlo and Molecular Dynamics Simulations in Polymer Science*; Oxford University Press: New York, 1995.
(90) Micka, U.; Holm, C.; Kremer, K. *Langmuir* **1999**, *15*, 4033−4044.
(91) Carrillo, J.-M. Y.; Dobrynin, A. V. *Macromolecules* **2011**, *44*, 5798−5816.
(92) Košovan, P.; Limpouchová, Z.; Procházka, K. *J. Phys. Chem. B* **2007**, *111*, 8605−8611.
(93) Stevens, M. J.; Kremer, K. *J. Chem. Phys.* **1995**, *103*, 1669−1690.
(94) Darden, T.; York, D.; Pedersen, L. *J. Chem. Phys.* **1993**, *98*, 10089−10092.
(95) Grest, G. S.; Kremer, K. *Phys. Rev. A: At., Mol., Opt. Phys.* **1986**, *33*, 3628−3631.
(96) Plimpton, S. *J. Comput. Phys.* **1995**, *117*, 1−19, http://lammps.sandia.gov,.
(97) Humphrey, W.; Dalke, A.; Schulten, K. *J. Mol. Graphics* **1996**, *14*, 33−38, http://www.ks.uiuc.edu/Research/vmd/,.
(98) Rosi-Schwartz, B.; Mitchell, G. R. *Polymer* **1996**, *37*, 1857−1870.
(99) Chu, B.; Wu, C.; Bucks, W. *Macromolecules* **1989**, *22*, 831−837.
(100) Ullner, M.; Jönsson, B.; Peterson, C.; Sommelius, O.; Söderberg, B. *J. Chem. Phys.* **1997**, *107*, 1279−1287.
(101) Šolc, K. *J. Chem. Phys.* **1971**, *55*, 335−344.
(102) Theodorou, D. N.; Suter, U. W. *Macromolecules* **1985**, *18*, 1206−1214.
(103) Arkin, H.; Janke, W. *J. Chem. Phys.* **2013**, *138*, 054904.
(104) Šolc, K.; Stockmayer, W. H. *J. Chem. Phys.* **1971**, *54*, 2756−2757.
(105) Allen, M. P.; Tildesley, D. J. *Computer Simulation of Liquids*; Clarendon Press: New York, 1989.
(106) Dobrynin, A. V. *Macromolecules* **2006**, *39*, 9519−9527.
(107) Liu, S.; Ghosh, K.; Muthukumar, M. *J. Chem. Phys.* **2003**, *119*, 1813−1823.
(108) Welch, C.; Labouriau, A.; Hjelm, R.; Orler, B.; Johnston, C.; Kim, Y. S. *ACS Macro Lett.* **2012**, *1*, 1403−1407.
(109) Fan, Y.; Tongren, D.; Cornelius, C. J. *Eur. Polym. J.* **2014**, *50*, 271−278.

DOI: 10.1021/acs.macromol.5b02158
Macromolecules 2016, 49, 1479−1489